

Cite this article: WANG X C, GUI H B, LIU Y. Numerical simulation of three-dimensional flow around a circular cylinder of finite length[J/OL]. Chinese Journal of Ship Research, 2018, 13(2). <http://www.ship-research.com/EN/Y2018/V13/I2/27>. DOI: 10.3969/j.issn.1673-3185.2018.02.004.

Numerical Simulation of three-dimensional flow around a circular cylinder of finite length

WANG Xiacong, GUI Hongbin, LIU Yang

School of Naval Architecture, Harbin Institute of Technology, Weihai 264209, China

Abstract: [Objectives] In this paper, in order to study the flow characteristics and mechanism of three-dimensional flow around a circular cylinder of finite length, [Methods] a numerical simulation using a Large Eddy Simulation (LES) and vortex structural classification technology is carried out, and the accuracy of the simulation is proven. [Results] When analyzing the flow field, it is found that the length of the recirculation zone is smaller for a circular cylinder of finite length. In addition, the downstream from the free end can suppress the common phenomenon of Karman-Vortex-Street which leads to a loss of drag-coefficient. Compared with the fixed wall at the bottom, the free end surface has a higher influence on the onstream-wise velocity. The 'mushroom' vortex appears in pairs and two original points exist on the free end. The circular cylinder of finite length appears to be strongly three-dimensional with a lower drag-coefficient. Moreover, there is a tip vortex behind the free end and a horseshoe vortex in the cylinder-wall junction. [Conclusions] The results of this paper give a relatively comprehensive description of the flow characteristics of a circular cylinder of finite length, and can provide useful references for relevant research.

Key words: finite length; flow around circular cylinder; downstream; free end surface; Large Eddy Simulation (LES)

CLC number: U664.33

0 Introduction

The phenomenon of flow around a body is widespread in the natural world. Whether land structures (such as a cable on a bridge) or various columnar structures in the ocean (such as the rig leg of offshore drilling platform) will be affected by it. Flow around a circular cylinder will generate vortex shedding and induce pulsating load of the fluid and structural vibration^[1], which will cause vortex-induced vibration. When the vibration is severe, it will cause structural damage such as fatigue to the structures^[2], so studying the classic phenomenon of flow around a circular cylinder is of great significance. Up to now, although the academic community has done a lot of research on the classic fluid mechanics problem of flow around a circular cylinder, the research on the finite cylinder (FC) is rare. Given the effect of down-

wash of the upper end surface of the cylinder, the flow around an FC is very different from the flow around an infinite cylinder (IFC), and its three-dimensional characteristic is significant^[3]. Therefore, it is very necessary to study it.

First, in terms of experiments, scholars in China and abroad mainly studied the change laws of aspect ratio (AR) of cylinder, Strouhal number St of free end surface, and drag coefficient of free end. Park et al.^[4] used particle image velocimetry (PIV) technique to experimentally analyze an FC with Reynolds number $Re=7.5\times 10^3$. It was found that tip vortices appear at the free end of the cylinder in pairs. After analysis, the tip vortices were found to be generated due to the interactions of the downwash flow of the end face and the flow around of the cylinder. Benitz et al.^[5] performed a series of aspect ratio experiments and numerical simulations for an FC un-

Received: 2017 - 09 - 11

Author(s): WANG Xiacong, male, born in 1993, master degree candidate. Research interests: three-dimensional flow around a circular cylinder and vortex-induced vibration. E-mail: wangxcesky@163.com
GUI Hongbin (Corresponding author), male, born in 1967, Ph.D., professor. Research interests: ship structural design, structural vibration and noise control. E-mail: guihongbin@sina.com



der Reynolds number $Re=2.9 \times 10^3$ and Froude number $Fr=0.65$. Compared with the IFC, the drag coefficient of flow around an FC is smaller, and the decrease of drag coefficient is the most obvious when $AR=2$. In addition, when $AR < 3$, the flow of downwash, due to the free end effect, will be completely suppressed by Karman Vortex Street, as shown in Fig. 1.

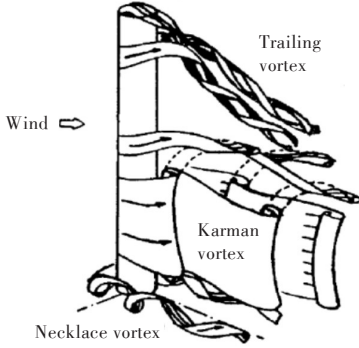


Fig.1 Flow model of FC^[6]

Second, in terms of numerical simulation, Fröhlich et al.^[6] used the LESCOCC2 code to solve the incompressible N-S equations by the large eddy simulation (LES) method and calculated FCs with $AR=2.5$. In the simulation, subgrid scale (SGS) models of Smagorinsky model (SM) and Dynamic Smagorinsky model (DSM) are used. The results show that DSM has obvious defects for the simulation of the FC in the current aspect ratio, making the eddy viscosity in computation so large that the boundary condition of the lower wall changes from the boundary layer to the symmetry plane; while the SM can perform the simulation better. Based on the immersed boundary method, Palau-Salvador et al.^[7] used LES to conduct tests and simulation analysis on two kinds of FCs ($AR=2.5, 5$) under two working conditions of Reynolds number ($Re=4.3 \times 10^4, 2.2 \times 10^4$). It was found that alternating vortex shedding of shorter cylinder only occurs near the wall and it is unstable.

Based on the results of previous studies, this paper proposes to simulate an FC and an IFC with the same geometry in the corresponding computational domain and select the condition of $Re=3.9 \times 10^3$ which has been studied more by former studies, to validate the feasibility of the proposed method. Then, the time-averaged characteristics and instantaneous characteristics of FC flow field are analyzed to simulate the "horseshoe" vortex, tip vortex, and "mushroom" vortex that are unique to the FC. Finally, the obtained data and flow field characteristics are compared with the simulation results of an IFC to understand the three-dimensional characteristics of

the FC flow field and the influence of the free end surface and the fixed wall on the flow field. The reason for the loss of the FC drag coefficient is expected to be explained from the perspective of the vortex shedding of the flow field, to provide a reference for the study of vibro-acoustic problems in a half-space structure.

1 Mathematical model

1.1 Governing equations

In this paper, the turbulence model of LES is used for numerical simulation. The basic principle of this method is to filter the vortices in space, in which the large vortex adopts the direct simulation method, while the small vortex adopts the SGS model to simulate the impact on large vortex. When considering the viscous, incompressible water as the fluid medium, the N-S equation can be written as:

$$\frac{\partial u_i}{\partial t} + \frac{\partial(u_i u_j)}{\partial x_j} = -\frac{1}{\rho} \frac{\partial p}{\partial x_i} + \nu \frac{\partial^2 u_i}{\partial x_i \partial x_j} \quad (1)$$

where ρ is the fluid density; p is the pressure; ν is the kinematic coefficient of viscosity of fluid; u_i and u_j are the velocity components; x_i and x_j are the displacement components; t is the time. The vortices smaller than the filter function are filtered from the turbulent transient motion equation and the equation of motion describing the large-eddy flow field is obtained by decomposition. N-S equation and the continuity equation processed by the filter function, namely, the control equations of LES, are:

$$\frac{\partial}{\partial t}(\rho \bar{u}_i) + \frac{\partial}{\partial x_i}(\rho \overline{u_i u_j}) = -\frac{\partial \bar{p}}{\partial x_i} + \frac{\partial}{\partial x_j}(\mu \frac{\partial \bar{u}_i}{\partial x_j}) - \frac{\partial \tau_{ij}}{\partial x_i} \quad (2)$$

$$\frac{\partial \bar{p}}{\partial t} + \frac{\partial}{\partial x_i}(\rho \bar{u}_i) = 0 \quad (3)$$

Where \bar{u}_i , $\overline{u_i u_j}$ and \bar{p} are relative parameters after filtering of filter function, respectively; $\tau_{ij} = \rho \overline{u_i u_j} - \rho \bar{u}_i \bar{u}_j$ is SGS stress, to describe the impact of small vortex on large one. Since τ_{ij} itself is unknown, SGS model needs to be constructed to close the control equations.

SM is adopted in this paper and subgrid stress is defined as:

$$\tau_{ij} - \frac{1}{3} \tau_{kk} \delta_{ij} = -2\mu_t \bar{S}_{ij} \quad (4)$$

where τ_{kk} is the isotropic SGS stress; δ_{ij} is the Kronecker symbol; $\mu_t = (C_s \Delta) |\bar{S}|$ is SGS turbulent viscosity, where C_s is the Smagorinsky constant and under outflow conditions, $C_s = 0.2$, $\Delta = (\Delta_x \Delta_y \Delta_z)^{1/3}$,

$\Delta_x, \Delta_y, \Delta_z$ are the grid sizes along x, y and z axes respectively, and Δ is the filter size. $|\bar{\mathcal{S}}| = \sqrt{2\bar{\mathcal{S}}_{ij}\bar{\mathcal{S}}_{ij}}$, where $\mathcal{S}_{ij} = \frac{1}{2}(\frac{\partial \bar{u}_i}{\partial x_j} + \frac{\partial \bar{u}_j}{\partial x_i})$ is the tensor expression of deformation rate of solvable scale x_i .

1.2 Geometric model and grid division

In order to compare the characteristics of flow around an FC, this paper selects FC and IFC models with the same geometry for computation and analysis, as shown in Fig. 2. In Fig. 2(a), the span-wise height of the computational domain of IFC is equal to the height of the cylinder. In Fig. 2(b), the span-wise height of the computational domain of FC is greater than the cylinder height.

ratio of the model is 5.23%. Since the free end surface of the cylinder and the upper surface of the fluid domain must allow enough space to accurately capture the flow conditions near the free end surface, taking into account the development of the flow field above the free end, the distance between the free end surface and the upper surface of the flow field domain is about $3D$.

Fig. 3 shows the grid division in the computational domain of the cylinder. The top view of the IFC is the same as that of the FC. The O-shaped grid is used to perform local refinement on the periphery of the cylinder. To effectively monitor the flow at the free end of the FC, the grid division in this area is also locally refined to accurately capture the flow characteristics.

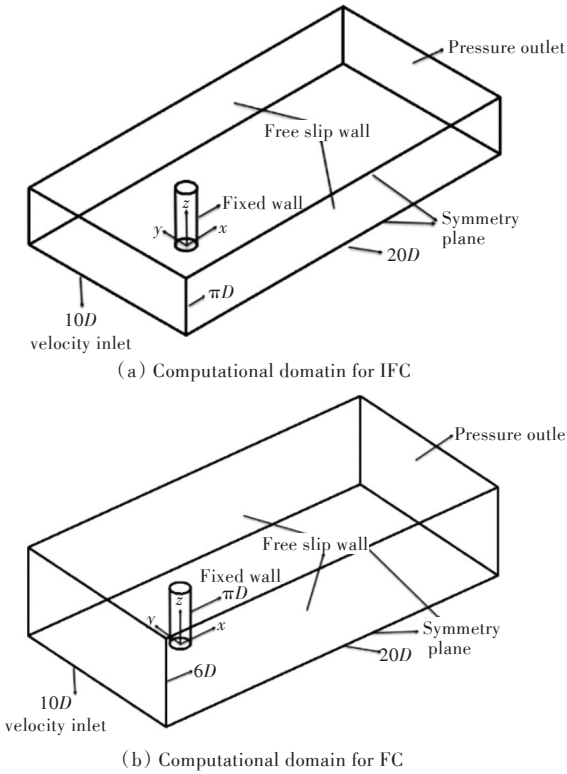
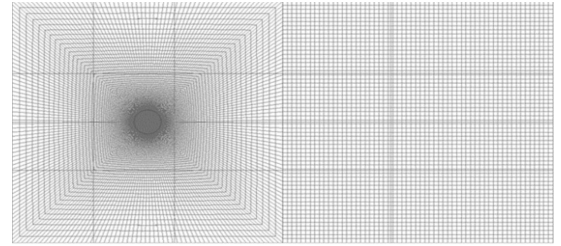
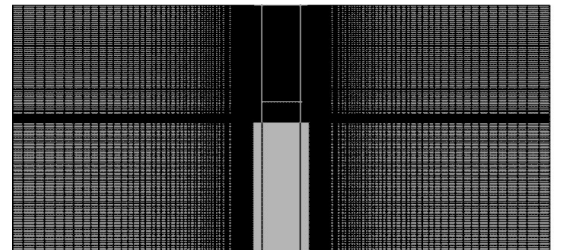


Fig.2 Model of computational domain for FC and IFC

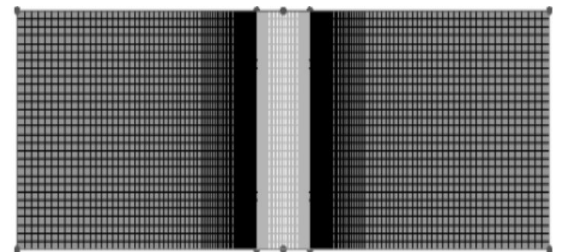
The above geometric model adopts the Cartesian coordinate system as the reference coordinates of the computational domain. In the figure, x, y and z represent the streamwise, transverse-flow and spanwise directions respectively. The origin of the coordinates is at the ground center of the cylinder. The size of the FC computational domain is $10D \times 20D \times 6D$; the size of the computational domain of IFC is $10D \times 20D \times \pi D$; and D is the feature size, namely, the diameter of the cylinder. The span-wise height of this cylinder is πD ; the distance from the center of the cylinder to the upstream inlet is $5D$; and the distance to the downstream exit is $15D$. The blockage



(a) Top view of grid of FC and IFC



(b) Profile map of FC



(c) Profile map of IFC

Fig.3 Grid division of computational domain for FC and IFC

1.3 Boundary conditions and time step selection

The boundary conditions are set as velocity inlet, pressure outlet, wall, and symmetry plane, which correspond to the inlet surface, outlet surface, side surface, and upper and lower walls of the geometry, respectively.

For the explicit computation of the n -dimensional problem, the time step should satisfy the Cou-

rant–Friedrichs–Lewy (CFL) condition, and its expression is

$$C = \Delta t \sum_{i=1}^n \frac{u_i}{\Delta i} \leq C_{\max} \quad (5)$$

where C is Courant number, with $C_{\max} = 1$; u_i is the flow velocity of direction i ; Δi is minimum computational grid size here; Δt is computational time step.

For the computation in this paper, $n=1$, so it only needs to satisfy that: $u(\Delta t/\Delta x) \leq 1$. At this time, u is the streamwise velocity U_0 . The non-dimensional time is set as: $\Delta t^* = \Delta t D/U_0 = 5.13 \times 10^{-4}$. Then the computational time step Δt is chosen as 2.5×10^{-3} s, and $C=0.975$, so the conditions are satisfied.

1.4 Model validation

In order to effectively validate the accuracy of the computation, the computational domains for FC and IFC are computed under the same initial conditions. Under the Fluent computational fluid dynamics software, the SIMPLE format for pressure–velocity coupled solution is used and the difference scheme uses center difference. The Reynolds number Re is 3.9×10^3 with the far–point flow velocity and the cylinder diameter as the characteristic parameters. The results are compared with the results of previous experiments and numerical simulations, as shown in Table 1. In the table, Sim1 refers to the numerical simulation results obtained by Reference [8]. EXP1, EXP2 and EXP3 refer to the experimental results of References [9], [10] and [5], respectively.

Table 1 Comparison of numerical simulation and experimental results provided by the literatures

Example	Grid number	Re	AR	\bar{C}_d	C_{lrms}	St	SGS
IFC0	509 800	3.9×10^3	–	1.078	0.124	0.21	SM
IFC1	619 500	3.9×10^3	–	1.026	0.116	0.21	SM
IFC2	619 500	3.9×10^3	–	1.141	0.126	0.22	DSM
IFC3	800 000	3.9×10^3	–	1.028	0.116	0.21	SM
Sim1	–	3.9×10^3	–	0.99	0.11	0.21	–
FC0	1 000 000	3.9×10^3	π	0.746	0.063	0.16	SM
FC1	1 822 972	3.9×10^3	π	0.784	0.053	0.11	SM
FC2	1 822 972	3.9×10^3	π	0.832	0.058	0.11	DSM
FC3	2 400 000	3.9×10^3	π	0.782	0.050	0.11	SM
EXP1	–	3.2×10^4	2	0.78	–	–	–
EXP2	–	4.7×10^4	2	0.73	–	0.122	–
EXP3	–	2.9×10^3	π	0.77	–	–	–

The table lists the time–averaged drag coefficient \bar{C}_d , root–mean–square value of lift coefficient C_{lrms} ,

and vortex shedding frequency related parameter Strouhal number St . The equation of Strouhal number St is:

$$St = fD/U_0 \quad (6)$$

where f is the main frequency of vortex shedding.

From Table 1, it can be seen that in the same SGS model, the results of IFC example IFC1 and FC example FC1 are very close to the experimental results. Although the results of IFC example IFC3 and FC example FC3 are closer, compared to the increase in computational resource consumption, the IFC example IFC1 and the FC example FC1 are more reasonable schemes.

To validate the conclusion of the SGS stress model in Reference [6], this paper has computed relevant parameters in the SM and DSM for FC and IFC. Through comparison, it has been found that the SM could indeed more accurately simulate the flow around of a circular cylinder in the sub–critical region for the current working conditions. In the subsequent calculation, whether it is computation for the flow around FC or IFC, the SM SGS stress model is selected in this paper, and the SM constant C_s is 0.2^[11]. This paper compares the computation results with previous experimental results and finds that under IFC1 and FC1 conditions, the results obtained are very close to the experimental results and are the closest to the physical quantity \bar{C}_d as the most accurate measurement^[6]. Subsequent computations in this paper take IFC1 and FC1 working conditions for numerical operation.

In order to further validate the correctness of the examples, the time–averaged streamwise velocity u_x and the circumferential pressure coefficient C_p distribution along the centerline ($y=0, z=\pi D/2$) of the FC and IFC are listed, respectively. The comparison with the computation results of Reference [12] is shown in Fig. 4. The computation equation of the pressure coefficient C_p is:

$$C_p = (p - p_0)/0.5\rho U_0^2 \quad (7)$$

where p and p_0 are monitoring point pressure and infinite point pressure, respectively.

From Fig. 4, the error between the computation results and the results of Reference [12] is within 3%, which further shows that the selection of computational conditions in this paper is reasonable. In addition, by comparing the computation results of the IFC, it can be found that the streamwise velocity of the FC and IFC becomes positive at $x/D \approx 1.875$ and 2.25, which means that the recirculation zone of

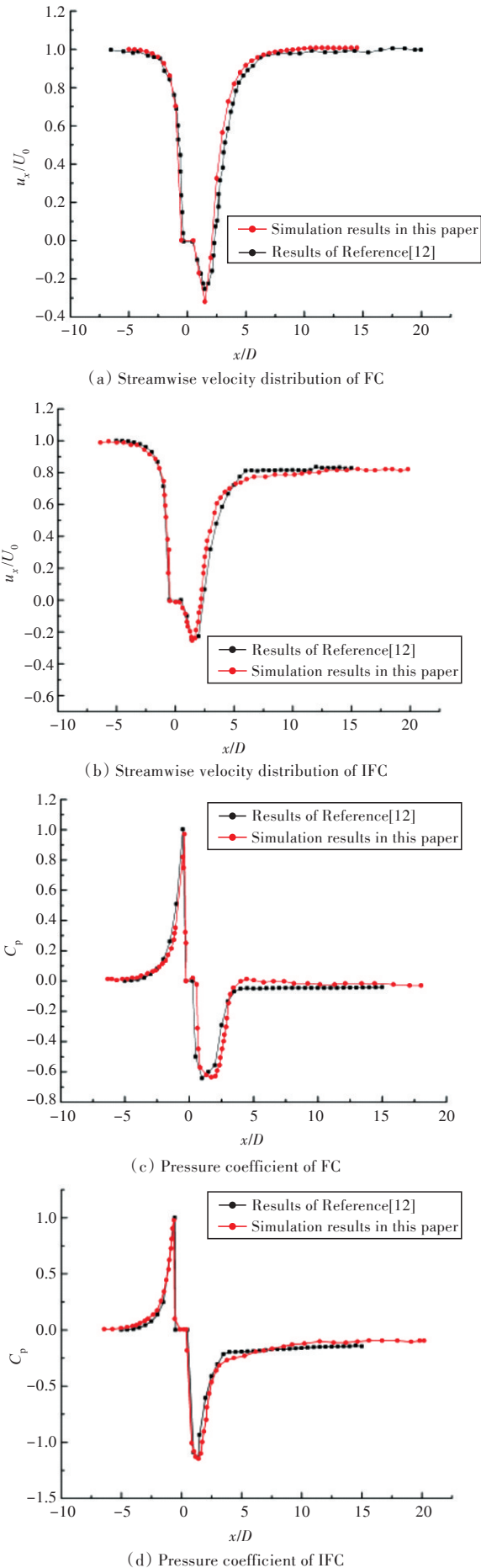


Fig.4 Distribution of streamwise velocity u_x and pressure coefficient C_p for FC and IFC

the FC is smaller, and the influence of downwash caused by the free end surface on the recirculation zone leads to the loss of the streamwise drag coefficient C_d . It is consistent with the results of Table 1.

2 Characteristic analysis of three-dimensional flow

2.1 Characteristic analysis of time-averaged flow field

Fig. 5 shows the steady-state time history curves of the lift and drag coefficients of FC and IFC. It can be seen from the figure that the time-averaged drag coefficient \bar{C}_d of FC is 23.6% smaller than that of IFC. The existence of the free end significantly changes the force of the cylinder, further illustrating the interference of the downwash on the flow field of flow around the circular cylinder. In addition, compared to the IFC, the lift coefficient C_l of the FC has a smaller peak value, and it is also more irregular. Considering the fact that the actual geometrical dimensions of the two cylinders are the same, it shows that under the FC computational domain, the

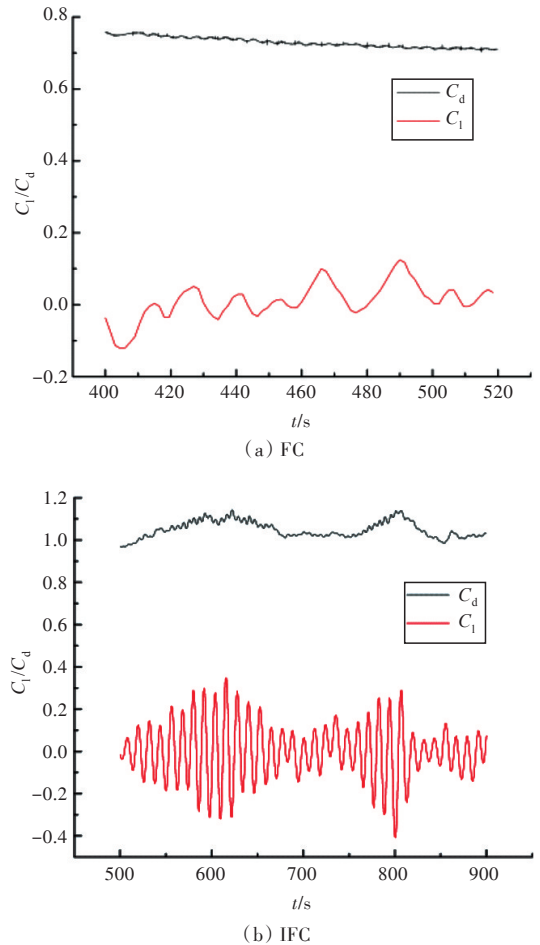


Fig.5 Distribution of the time-dependent lift and drag coefficient for FC and IFC

downwash action at least partially disturbs the Karman Vortex Street shown by the original sub-critical region.

In order to study the influence of the free end surface of the cylinder on the downwash of the fluid, the cylinder will be horizontally truncated at the spanwise center of the cylinder, with the leading edge point as the initial monitoring point ($\theta = 0^\circ$). Circumferential monitoring points are uniformly arranged along the main flow direction from 0° to 180° with the spacing of 10° and the time-averaged curves of pressure coefficient at each monitoring point are calculated. To compare with an IFC, an equal number of monitoring points is set at the same monitoring positions (namely, the spanwise center of the IFC). The test results are shown in Fig. 6.

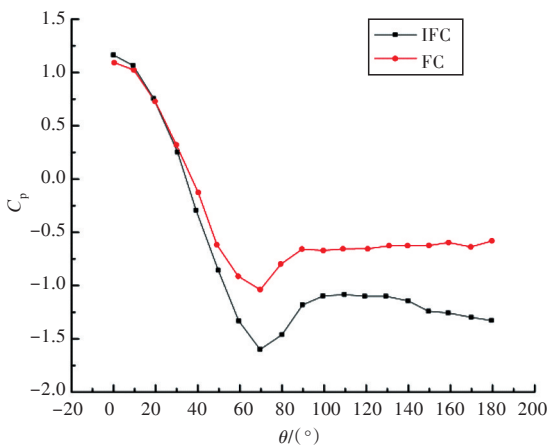


Fig.6 Distribution of pressure coefficient around circumference

It can be seen from Fig. 6 that FC and IFC have the same separation angle at the middle position. The difference is that, for the pressure coefficient C_p , the difference between the FC and the IFC is 35%. It can be seen that for FC with a smaller aspect ratio, the downwash at the end face can cause great disturbance to the flow, which can bring about great changes to the flow field. In addition, due to the effect of the downwash, the flow of cylinder wake near the wall is inhibited.

In order to further study the effect of the free end surface and the fixed wall on the wake flow in the near wall region of the cylinders, more than 60 monitoring points are set uniformly for the FC and IFC on the vertical straight line with $y=0$, $x=D$ to monitor the streamwise velocity u_x . The result after the non-dimensional treatment is shown in Fig. 7 (in the figure, h is the span-wise height of the cylinder). It can be seen from the figure that, for the IFC, at $x=D$, the streamwise velocity u_x is negative. Combined with the distribution curve of the streamwise

velocity u_x along the x -direction, it is shown that the recirculation zone of the cylinder is greater than D , which is consistent with the analysis of the pressure coefficient in the previous paper. At the same time, in the region of $z \leq 0.8h$, regardless of the FC or IFC, u_x values are both negative, but when $z \geq 0.8h$, the velocity of FC quickly rises; from the free end surface to the position, where is about $1.2D$ from the free end surface, the velocity becomes the flow velocity at infinity. Further analysis of relative difference between the FC and the IFC at $z/h=0$ and $z/h=\pi$ shows that the influence of the free end on the streamwise velocity u_x is greater than that of the fixed wall.

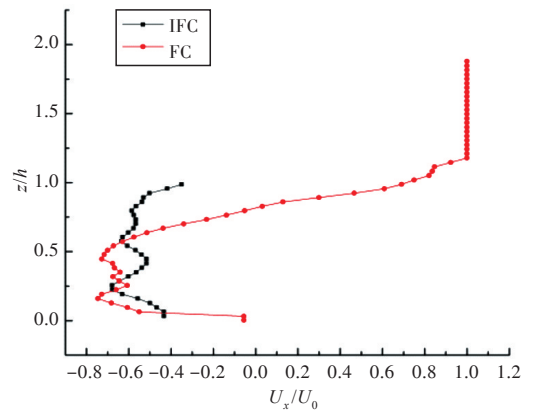


Fig.7 Distribution of streamwise velocity u_x around z axis for FC and IFC

2.2 Characteristic analysis of instantaneous flow field

During the actual flow of FC, the lower wall, that is, the cylindrical fixed wall, is not a smooth wall. The non-slip characteristic of the fixed wall results in the "horseshoe" vortex. To obtain the tip vortex and "horseshoe" vortex at the same time, the upper and lower plane symmetry conditions in the original FC computation are changed to the non-slip of the lower wall in this paper, and the flow field of flow around the FC is recalculated.

In order to clearly obtain the flow of vortex shedding behind the cylinder, the Q -criterion is used to define the vorticity as follows:

$$Q = \frac{1}{2} \left[\left\| S^2 \right\| - \left\| \boldsymbol{\Omega}^2 \right\| \right] \quad (8)$$

$$S_{ij} = \frac{1}{2} \left(\frac{\partial u_i}{\partial x_j} + \frac{\partial u_j}{\partial x_i} \right) \quad (9)$$

$$\boldsymbol{\Omega}_{ij} = \frac{1}{2} \left(\frac{\partial u_i}{\partial x_j} - \frac{\partial u_j}{\partial x_i} \right) \quad (10)$$

where S_{ij} is strain tensor; $\boldsymbol{\Omega}_{ij}$ is computation vortic-

ity.

In the three-dimensional Cartesian coordinate system, the simplified equation is:

$$Q = -\frac{1}{2} \left[\left(\frac{\partial u}{\partial x} \right)^2 + \left(\frac{\partial v}{\partial y} \right)^2 + \left(\frac{\partial w}{\partial z} \right)^2 \right] - \frac{\partial u}{\partial y} \frac{\partial v}{\partial x} - \frac{\partial u}{\partial z} \frac{\partial w}{\partial x} - \frac{\partial v}{\partial z} \frac{\partial w}{\partial y} \quad (11)$$

where u , v and w are velocity components in three directions, respectively.

Fig. 8 shows the distribution of vorticity iso-contours based on the Q -criterion. Fig. 8(a) shows the vorticity iso-contours of the tip vortex of free end surface at two moments. The development of the vorticity at different moments can be seen from the figure; the tip vortices appear in pairs; and the vortex separation angle at the top surface is approximately 70° . Fig. 8(b) shows the vorticity iso-contours at the spanwise center of the cylinder. It can be seen from the figure that the vortices no longer follow the standard Karman Vortex Street distribution, and the upper and lower vortices are no longer symmetrical. It can be seen that the free end has indeed affected the development of the vortices in the middle, which also confirms the conclusions during the previous analysis of the lift and drag coefficients. Fig. 8(c) presents the vorticity iso-contours of the fixed cylindrical wall; from the figure, due to the simultaneous consideration of the non-slip characteristic of the bottom surface, the bottom vortex flow is very complex, but in the front end of the cylinder, the vortex line of "horseshoe" vortices can be clearly seen. It is worth noting that the bottom surface of the cylinder is less affected by the downwash, so it retains certain

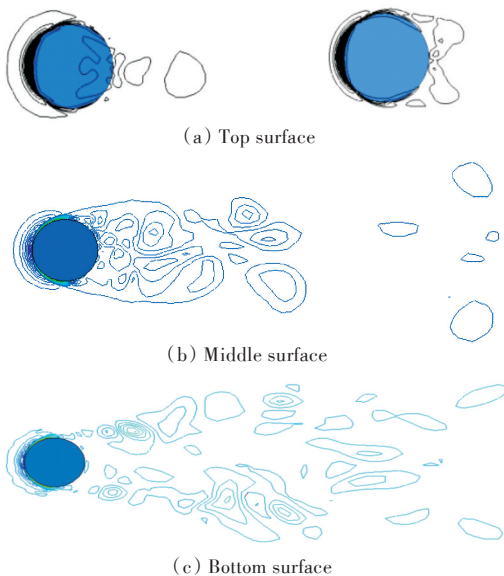


Fig.8 Distribution of iso-contours for vorticity of FC according to Q -criterion

amount of vortex shedding property similar to IFC. This also indirectly shows that for $AR=\pi$ cylinders, the downwash does not completely disrupt the flow field of the entire cylinder. From the bottom of the cylinder to half of its spanwise height, Karman Vortex Street is still the main component of the flow.

Fig. 9 shows the contours for x -direction velocity component of free end surface of FC and a partial enlarged view of free end surface streamlines. From the figure, the free end surface begins to generate vortices from the leading edge. The vortices develop gradually, cover the free end surface and form "mushroom" vortices. The vortex development area accounts for about $2/3$ of the length of the free end surface. This shows that after the fluid separated from the cylindrical leading edge is convoluted at $2/3$, the rest of the fluid continues to flow forward, with no reattachment. In the final downward direction of the free end, the fluid continues to be divided into two parts: One flows towards the wall of the cylinder and forms a convolution, that is, tip vortex. It is just this type of tip vortex that constitutes the main flow characteristics of FC together with the Karman Vortex Street; the other part continues to flow backwards, but its flow trajectory is no longer straight, but flows in the downward direction.

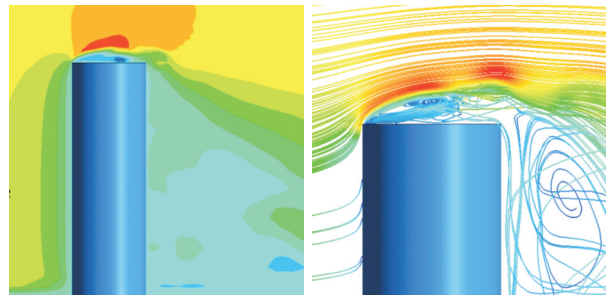


Fig.9 Contours of streamwise velocity for FC

Fig. 10 shows the diagram of the limiting streamlines on cylinder wall. In Fig. 10(a), the limiting streamlines converge into a straight line along the spanwise direction, which is the line formed by the separation points of the flow around the cylindrical wall. The free-end limiting streamline diagram of the top surface as shown in Fig. 10(b) can clearly show two original streamline points. The points are the original points of the "mushroom" vortex generation. It is here that the separated fluids respectively convolute along the midline to both sides to form vortices, which is consistent with the study results in Reference [2].

In order to understand three-dimensional vortex structure of the cylinder more clearly, the vorticity

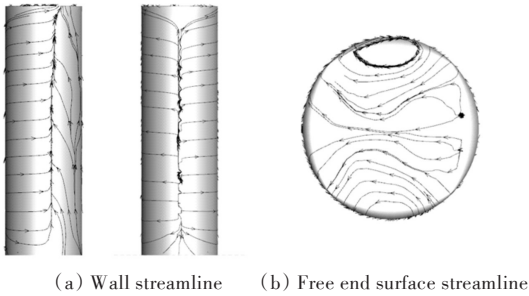


Fig.10 Diagram of cylinder's surface streamline

iso-contours based on the Q -criterion are obtained for FC and IFC, respectively, as shown in Fig. 11. It can clearly be seen from the figure that compared to the IFC, the vortex structure of FC is more complex but relatively weaker. The flow around FC is confined to a relatively small area, but the vortices of FC become gradually smoother toward the downstream region. As can be seen in Fig. 11(a) and Fig. 11(b), the recirculation zone of the FC is shorter due to the existence of the downwash effect, and the shape of the vortex section is clearly "triangular". This is consistent with the phenomenon that the streamlines in the wake flow behind the cylinder develop diagonally downward in the previous streamline diagram, but there is no such phenomenon in the IFC. The flow field behind the cylinder is relatively uniform, and the section is a standard "rectangle". It is just because of the above reasons that loss of drag coefficient C_d of the FC is created. In addition to the wake vortex structure, it can be seen from Figs. 11(c) and 11(d) that a "horseshoe" vortex can be clearly observed at the junction of the cylinder body and the ground. It is caused by the non-slip characteristic of the bottom surface.



(a) Side view of vorticity for FC



(b) Side view of vorticity for IFC



(c) Top view of vorticity for FC



(d) Top view of vorticity for IFC



(e) Front view of vorticity of FC



(f) Front view of vorticity of IFC

Fig.11 Vortical structures revealed by isosurface of the Q -criterion($Q=6$)

3 Conclusions

In this paper, based on the numerical simulation of LES, the FC and IFC under $Re=3.9 \times 10^3$ working conditions are simulated numerically. Through comparison with the literature study results, the correctness of the proposed method is proved. In the time domain, this paper compares the FC with the IFC in terms of flow field velocity, drag coefficient, lift coefficient and transient flow field contours. The conclusions are as follows:

1) Relative to IFC, the flow of FC is more complicated, and its drag coefficient is 23.6% smaller. The monitoring results for the circumferential pressure coefficient show that the pressure coefficient of FC is 35% smaller. The main reason is that the downwash of the free end surface changes the original flow pattern of Karman Vortex Street, which weakens the wake flow. At the same time, the lift coefficient of FC is also smaller than that of IFC, which shows that the FC has a significant inhibitory effect on the cylinder force. In the analysis of the streamwise velocity of FC and IFC in vertical direction, it is concluded that the influence of the free end surface on the FC is larger than that of the fixed wall.

2) Based on the Q -criterion ($Q = 6$), the finite-length flow field is analyzed, and the vorticity iso-contours are analyzed on three planes ($z = \pi D$, $z = 1/2\pi D$, $z = 0$). It is found that the range of influence of the free end on the wake flow at the trailing edge of the cylinder exceeds half of the height of the cylinder under the condition of $AR=3$. At the bottom surface of the cylinder, due to the fixed wall, the horseshoe vortex peculiar to the FC will appear on the leading edge of the cylinder bottom. The vortex also has a certain influence on the flow at the bottom of the cylindrical trailing edge, resulting in a very complex bottom flow field, but the impact on the Karman Vortex Street is relatively smaller relative to the top surface. According to the analysis of the streamwise velocity contours and streamlines on the middle surface of the cylinder ($y=0$), it can be found that the development area of the top vortex, namely, the "mushroom" vortex, accounts for about 2/3 of the length of the free end surface. Observing the distribution of the free end streamlines can clearly obtain the two original streamline points. And, the fluid that bypasses the free end is divided into two parts: One part is reattached to the wall to form the tip vortex, and the other part flows in the diagonally downward direction. The subsequent vorticity isosurface indirectly proved this point.

3) Also based on the Q -criterion, vorticity isosurface are constructed for FC and IFC, respectively. It can be seen that the flow of FC is weaker than that of IFC, the recirculation zone is shorter, and the existence of downwash flow causes that its interface flow field is not "rectangular" like in IFC, but shows a "triangular" shape.

References

- [1] WANG L, LI T Y, ZHU X, et al. Improved immersed boundary lattice Boltzmann method and simulation of flow over rotating cylinder[J]. Chinese Journal of Ship Research, 2016, 11(6): 97-103 (in Chinese).
- [2] NAUDASCHER E, ROCKWELLD. Flow-induced vibrations: an engineering guide: IAHR hydraulic structures design manuals 7[M]. Rotterdam: Balkema Publishers, 1994.
- [3] SUMNER D. Flow above the free end of a surface-mounted finite-height circular cylinder: a review [J]. Journal of Fluids and Structures, 2013, 43: 41-63.
- [4] PARK C W, LEE S J. Effects of free-end corner shape on flow structure around a finite cylinder[J]. Journal of Fluids and Structures, 2004, 19(2):141-158.
- [5] BENITZ M A, CARLSON D W, SEYED-AGHAZADEH B, et al. CFD simulations and experimental measurements of flow past free-surface piercing, finite length cylinders with varying aspect ratios[J]. Computers & Fluids, 2016, 136: 247-259.
- [6] FRÖHLICH J, RODI W. LES of the flow around a circular cylinder of finite height[J]. International Journal of Heat and Fluid Flow, 2004, 25(3): 537-548.
- [7] PALAU-SALVADOR G, STOESEER T, FRÖHLICH J, et al. Large eddy simulations and experiments of flow around finite-height cylinders [J]. Flow, Turbulence and Combustion, 2010, 84(2): 239-275.
- [8] WORNOM S, OUVRARD H, SALVETTI M V, et al. Variational multiscale large-eddy simulations of the flow past a circular cylinder: Reynolds number effects [J]. Computers & Fluids, 2011, 47(1):44-50.
- [9] KAWAMURA T, HIWADA M, HIBINO T, et al. Flow around a finite circular cylinder on a flat plate: cylinder height greater than turbulent boundary layer thickness [J]. Bulletin of JSME, 1984, 27 (232) : 2142-2151.
- [10] OKAMOTO S, SUNABASHIRI Y. Vortex shedding from a circular cylinder of finite length placed on a ground plane [J]. Journal of Fluids Engineering, 1992, 114(4):512-521.
- [11] WELLER H G, TABOR G, JASAK H, et al. A tensorial approach to computational continuum mechanics using object-oriented techniques [J]. Computers in Physics, 1998, 12(6): 620-631.
- [12] ZHANG H, YANG J M, XIAO L F, et al. Large-eddy simulation of the flow past both finite and infinite circular cylinders at $Re=3900$ [J]. Journal of Hydrodynamics (Ser. B), 2015, 27(2): 195-203.

[Continued on page 46]

